JAM CM Journal of Applied Mathematics and Computational Mechanics 2025, 24(4), 26-36
www.amcm.pcz.pl p-ISSN 2299-9965
DOI: 10.17512/jamcm.2025.4.02 e-ISSN 2353-0588

ANALYSIS OF RESONANT MODES AND LOCALIZATION PHENOMENA IN A TWO-DIMENSIONAL PERFORATED WAVEGUIDE

Konrad M. Gruszka, Kamila Pasternak

Faculty of Computer Science and Artificial Intelligence, Czestochowa University of Technology
Częstochowa, Poland
kgruszka@icis.pcz.pl, kamila.pasternak@pcz.pl

Received: 20 October 2025; Accepted: 1 December 2025

Abstract. This paper investigates the formation of resonant modes, within a two-dimensional silicon-based waveguide, intricately perforated with circular and square-type defects using the finite-difference time-domain method. The study systematically examines how the geometry of these perforations – specifically circles with a radius of 360 nm and squares of equivalent side length – influences the emergence and behavior of these modes. A particular focus is given to the influence of the defect shape on the modes, examining configurations where defects are circular, square, or absent (non-perforated segment acting as a defect).

MSC 2010: *65M06, 82D80*
Keywords: *FDTD, resonant modes, waveguide*

1. Introduction

In the case of periodic structures such as photonic crystals [1–3], when transmitting an electromagnetic wave through the system, its structure has a decisive influence on the characteristics of the transmitted wave. In particular, when a disturbance of the periodicity of the structure occurs in a photonic crystal, e.g. in the form of a point defect (vacancy), it often becomes a source of a localized Bloch mode (a type of resonance mode) [4]. Interestingly, this type of behavior is also observed in non-periodic structures, that is, in structures with finite spatial dimensions [5, 6]. Bloch modes in photonic crystals are localized states where the electromagnetic field is confined within a specific region of the structure. These modes arise when the frequency of the light wave matches the natural frequency of the photonic crystal, causing constructive interference and trapping the light in certain areas [7]. This confinement occurs due to the photonic bandgap, which prevents light from propagating in certain frequency ranges [8–10].

The research demonstrates that resonant modes occur across all studied configurations. By introducing and varying the defect shapes within the waveguide, this study

not only elucidates the role of defect geometry in the propagation of electromagnetic waves but also highlights the robustness of resonant mode formation in the presence of continuous and discrete structural variations.

2. FDTD governing equations

The FDTD method uses discrete time and space lattice points to solve Maxwell's equations numerically [11]. For the described system of a two-dimensional perforated waveguide with defects, the relevant Maxwell's equations can be discretized using the FDTD approach. The general forms of normalized Maxwell's equations, which are the foundation for FDTD simulations:

$$\frac{\partial \widetilde{\mathbf{D}}}{\partial t} = \frac{1}{\sqrt{\varepsilon_0 \mu_0}} \nabla \times \mathbf{H} \tag{1}$$

$$\widetilde{\mathbf{D}}(\omega) = \varepsilon_r^*(\omega) \cdot \widetilde{\mathbf{E}}(\omega) \tag{2}$$

$$\frac{\partial \mathbf{H}}{\partial t} = -\frac{1}{\sqrt{\varepsilon_0 \mu_0}} \nabla \times \widetilde{\mathbf{E}} \tag{3}$$

where ε_0 and μ_0 is the electric and magnetic permittivity respectively, ε_r^* is the complex relative dielectric constant, ω is the frequency, $\widetilde{\mathbf{D}}$ is the normalized electric flux density vector, $\mathbf{H}$ is the magnetic field vector and $\widetilde{\mathbf{E}}$ is the normalized electric field vector, and lastly t is time. In this case, normalization was applied using the following substitutions to the non-normalized general Maxwell's equations:

$$\widetilde{\mathbf{E}} = \sqrt{\frac{\varepsilon_0}{\mu_0}} \mathbf{E} \tag{4}$$

$$\widetilde{\mathbf{D}} = \sqrt{\frac{\varepsilon_0}{\mu_0}} \mathbf{D} \tag{5}$$

To take into account the dielectric material loss, the current density $\mathbf{J}$ is introduced, which is expressed by the formula:

$$\mathbf{J} = \sigma \mathbf{E} \tag{6}$$

where σ is the conductivity. Therefore, the ε_r^* from (2) is defined as:

$$\varepsilon_r^* = \varepsilon_r + \frac{\sigma}{j\omega\varepsilon_0} \tag{7}$$

Taking into account the above substitution, the equation (2) becomes:

$$\widetilde{\mathbf{D}}(\omega) = \varepsilon_r \widetilde{\mathbf{E}}(\omega) + \frac{\sigma}{j\omega \cdot \varepsilon_0} \widetilde{\mathbf{E}}(\omega) \tag{8}$$

As can be seen from above, the equation (2) is written in the frequency domain, while the FDTD method is realized in the *time domain*. Therefore, it is necessary to move from the frequency domain to the time domain. Using the Fourier theory, it can be shown that $1/(j\omega)$ in the frequency domain reduces to the integral equation in the time domain:

$$\widetilde{\mathbf{D}}(t) = \varepsilon_r \widetilde{\mathbf{E}}(t) + \frac{\sigma}{\varepsilon_0} \int_0^t \widetilde{\mathbf{E}}(t')dt' \tag{9}$$

Since time is discretized in FDTD, the integral will be approximated as a summation over small time steps Δt, which can be represented as follows:

$$\widetilde{\mathbf{D}^n}(t) = \varepsilon_r \widetilde{\mathbf{E}^n}(t) + \frac{\sigma \cdot \Delta t}{\varepsilon_0} \sum_{i=0}^{n} \widetilde{\mathbf{E}^i} \tag{10}$$

The presented problem of a defective waveguide will be considered in a two--dimensional space. In this case, the simulation can be defined in two ways, namely the case of TM – transverse magnetic mode or TE – transverse electric mode. In the latter case, the vectors $\widetilde{\mathbf{E}}_z$, $\mathbf{H}_x$ and $\mathbf{H}_y$ will be needed. The set of Maxwell's equations (1) (2) and (3) will then be simplified to the following form:

$$\frac{\partial \mathbf{D}_z}{\partial t} = \frac{1}{\sqrt{\varepsilon_0 \mu_0}} \left(\frac{\partial \mathbf{H}_y}{\partial x} - \frac{\partial \mathbf{H}_x}{\partial y} \right) \tag{11}$$

$$\mathbf{D}_z(\omega) = \varepsilon_r^*(\omega) * \mathbf{E}_z(\omega) \tag{12}$$

$$\frac{\partial \mathbf{H}_x}{\partial t} = -\frac{1}{\sqrt{\varepsilon_0 \mu_0}} \frac{\partial \mathbf{E}_z}{\partial y} \tag{13}$$

$$\frac{\partial \mathbf{H}_y}{\partial t} = \frac{1}{\sqrt{\varepsilon_0 \mu_0}} \frac{\partial \mathbf{E}_z}{\partial x} \tag{14}$$

In the above equations the normalization sign $\widetilde{\ }$ has been omitted for clarity of presentation; however, the **D** and **E** vectors remain normalized.

2.1. FDTD discretization

Within FDTD discretization, vector differential equations (11) to (14) are typically broken down into their cartesian components. For a 2D transverse magnetic mode analysis, assuming the electric field components only have a z-component (E_z), and

the magnetic field has only x and y components (H_x, H_y), the discretized equations can be approximated as:

$$\begin{aligned}\frac{\mathbf{D}_z^{n+1/2}(i,j)-\mathbf{D}_z^{n-1/2}(i,j)}{\Delta t} &= \frac{1}{\sqrt{\varepsilon_0\mu_0}}\left[\frac{\mathbf{H}_y^n\left(i+\frac{1}{2},j\right)-\mathbf{H}_y^n\left(i-\frac{1}{2},j\right)}{\Delta x}\right] \\ &\quad -\frac{1}{\sqrt{\varepsilon_0\mu_0}}\left[\frac{\mathbf{H}_x^n\left(i+\frac{1}{2},j\right)-\mathbf{H}_x^n\left(i-\frac{1}{2},j\right)}{\Delta y}\right]\end{aligned} \tag{15}$$

$$\frac{\mathbf{H}_x^{n+1}(i,j+\frac{1}{2})-\mathbf{H}_x^n(i,j+\frac{1}{2})}{\Delta t} = -\frac{1}{\sqrt{\varepsilon_0\mu_0}}\frac{\mathbf{E}_z^{n+1/2}(i,j+1)-\mathbf{E}_z^{n+1/2}(i,j)}{\Delta y} \tag{16}$$

$$\frac{\mathbf{H}_y^{n+1}(i+\frac{1}{2},j)-\mathbf{H}_y^n(i+\frac{1}{2},j)}{\Delta t} = \frac{1}{\sqrt{\varepsilon_0\mu_0}}\frac{\mathbf{E}_z^{n+1/2}(i+1,j)-\mathbf{E}_z^{n+1/2}(i,j)}{\Delta x} \tag{17}$$

where H_x, H_y are the magnetic field components, E_z is the electric field component, ε_0 and μ_0 represent the permittivity and permeability of the medium, respectively, Δt, Δx and Δy are the time step and spatial steps in the x and y directions, and finally n indicates the time step index. It is worth noting that, when discretizing space, a regular grid with equal spacing along the studied dimensions is employed. This reduce down to a square grid, in which the quantities Δx and Δy are equal. Lastly, time component Δt will be expressed by following equation:

$$\Delta t = \frac{\Delta x}{2\cdot c_0} \tag{18}$$

where c_0 is the speed of light in a vacuum. Here, it was decided to place Δx in the numerator, however, it should be remembered that when the grid is square it does not matter which discrete coordinate is used.

In Figure 1, a computational grid unit used to solve Maxwell's equations by discretizing both space and time is shown. It represents the spatial arrangement of electric and magnetic field components in a staggered manner, ensuring accurate modeling of electromagnetic wave propagation.

2.2. Studied system

The waveguide is constructed using silicon material with a dielectric constant of $\varepsilon_w = 11.8$. Three regular holes placed on each side of the defect are filled with air ($\varepsilon_a = 1$), and their radius is set to $0.36\,\mu$m for round hole defects and $0.36\,\mu$m as the side length when the holes are square. The lowest simulation resolution in our calculations was set to $40px/\mu$m for the cases where the defect radius was higher than $0.15\,\mu$m (doubled to $80px/\mu$m for $r = 0.15\,\mu$m and lower) and the used spatial grid was homogeneous in all simulation directions ($\Delta x = \Delta y$).

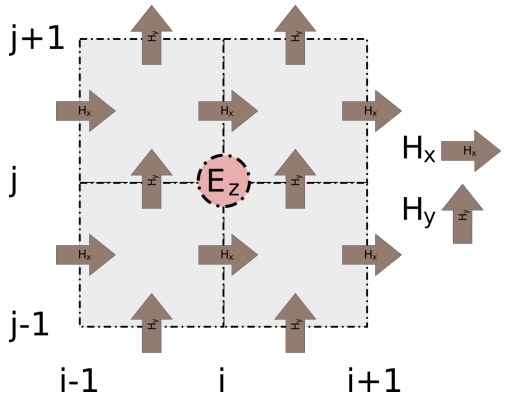

Fig. 1. Yee cell for FDTD calculation

$$\Delta x = \Delta y = \frac{1}{\text{resolution}} = \frac{1}{40}\,\mu\text{m} = 0.025\,\mu\text{m} \tag{19}$$

To calculate the timestep Δt in Meep, we used following equation:

$$\Delta t = S\Delta x = 0.5 \times 0.025 = 0.0125 \text{ (Meep time units)} \tag{20}$$

Because c is normalized and the Meep time unit is $= \dfrac{1\,\mu m}{c} = 3.33 \cdot 10^{-15}$ s, converting it to seconds: $\Delta t = 0.0125 \times 3.33 \cdot 10^{-15} \approx 4.16 \cdot 10^{-17}$ s. We have also carefully checked whether the Courant stability criterion is met for all the simulations. The waveguide environment is air. The Gaussian pulse source is located in the left part of the waveguide, and it is used to study the frequency response of the waveguide. The horizontal length of the waveguide is $13\,\mu$m, and its thickness is set to $1.2\,\mu$m. PML absorbing layers surrounding the entire simulation area are used for transmission studies, and implementation parameters in terms of order and grading profile were 3rd-order polynomial PML $(p = 3)$ and polynomial grading, described by $\sigma(x) = \sigma_{\max}\left(\dfrac{x}{d}\right)^p$, where: $p = 3$ – PML polynomial order, $d =$ PML thickness $= 1.0\,\mu$m, and x – distance from the beginning of the PML layer. The thickness of the layers is set to $1\,\mu$m. We carefully tested the required PML thickness in both cases to minimize wave scattering. Then, for both studied cases, a structure continuity defect was implemented in the system, lacking a central hole. This case was designated as "no hole". Next, the hole was placed in the central position, and then the size of this hole was systematically changed. A standard circular perforation is described by 29 points in the x direction (resolution), and taking into account the two-dimensional space, this is $29 \times 29 = 841$ points inside the perforation. In the case of the three smallest defects, a decision was made to double the simulation resolution (to $80px/\mu$m), which, for the smallest of them, resulted in a total of 64 points located inside the defect. For each of the structures generated in this way,

the transmission response of the system to an electromagnetic pulse with a Gaussian distribution was then examined. All the simulations were conducted in TE-mode.

3. Results

Figure 2 presents calculated normalized transmission for a waveguide with a circular shape defect. The normalization in both studied cases is done using transmission with a waveguide without any holes as a normalization factor. As can be seen, there is one mode for each defect size, located between the range $0.24[2\pi C/a]$ and $0.32[2\pi C/a]$. Below $0.24[2\pi C/a]$ and above $0.32[2\pi C/a]$, the visible transmission spectrum is due to the shape of the waveguide itself without significant influence due to periodic perforations. What is rather important in this case is how much of the waveguide space is not covered by the perforations, hence the differences occurring in this part as well. For larger electromagnetic wavelengths, the perforations are too small (the ratio between the incident wavelength and the physical size of the perforations is significant, leading to a situation called dipole approximation which leads to the fact that this wave "does not see" this structure and does not interact with it to a significant extent).

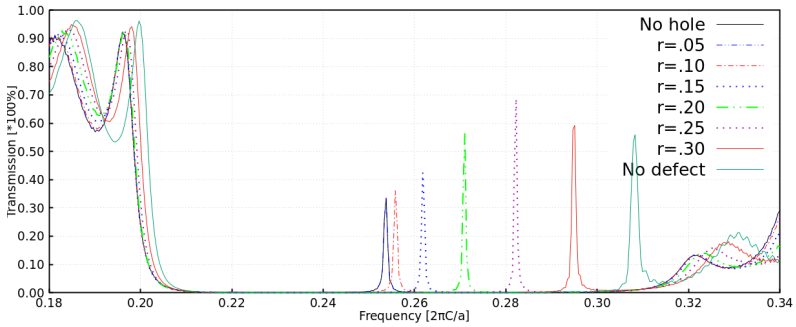

Fig. 2. Transmission for circle-shape holes waveguide

By the analysis of Figure 2, it can be observed that with the increase in the size of the defect (perforation) in the form of a circle, the position of this maximum and its intensity change. In this figure, the transmission curve marked as "no defect" represents the case in which the perforation continuity is preserved in the waveguide. This case is most similar to the classical ideal one-dimensional photonic crystal. The marking, "no hole" denotes a case in which the perforation does not occur at all, which can be considered as a defect in the continuity of the perforated waveguide structure. It is this lack of perforation that leads to the localization of the mode in the waveguide cavity thus created. All other designations visible in this figure mean that the perforation appears exactly in the center of the domain, i.e. in the middle of the waveguide, and where r is the perforation radius ($2R$ the side length in the case of a square-shaped perforation). As can be seen, in the case where there is no defect

(marked with a light blue line), the maximum transmittance peak lies on the far right side of the spectrum. The occurrence of a peak at this point in the spectrum is related to geometric parameters such as the free space between the perforation and the edge of the waveguide or the free space between adjacent perforations. These empty spaces also become places where resonant modes can appear, however, due to their generally small size, these modes can appear at quite high resonant frequencies (in this case $0.308[2\pi C/a]$). On the opposite side of the transmission spectrum lies the peak marked with a solid black line (its frequency is $0.253[2\pi C/a]$). This peak occurs in the case where there is no perforation in the central part of the waveguide. For this reason, it is the place with the largest cavity size. The larger the void size, the lower the resonance frequency of the mode and the longer the electromagnetic wavelength for which this mode occurs. The remaining peaks visible in Figure 2 occur in the area bounded by the two situations mentioned above. By observing the general relationship between the defect size and the frequency at which the transmittance peak occurs, it can be easily seen that the larger the defect diameter, the higher up in the frequency spectrum this peak is. A different type of relationship exists between the normalized intensity and the perforation size. In this case, the intensity initially increases until it reaches a maximum for the defect size $r = 0.24$, and then starts to decrease, reaching a minimum for the case without defect.

Figure 3 presents calculated normalized transmission for a waveguide with a rectangular shape defect. Comparable to the circular defect case (Fig. 2), normalization is done using the transmission of a waveguide without any holes as a normalization factor. In this case, the transmission spectrum exhibits notable differences due to the rectangular geometry of the perforations. As observed, there is one dominant mode for each defect size, located within the range $0.24[2\pi C/a]$ and $0.32[2\pi C/a]$. Below $0.24[2\pi C/a]$ and above $0.32[2\pi C/a]$, the spectrum is predominantly shaped by the waveguide geometry, with minimal influence from the periodic perforations.

Examination of Figure 3 reveals a similar dependence on defect size as in Figure 2, although certain geometric aspects of the rectangular perforations cause a change in the character visible in the transmission spectra. It can be observed that as the defect size increases, the position on the frequency scale of the transmission peak shifts, while its intensity changes. In this figure, the transmission curve labeled "no defect" (light blue line) represents the case in which the perforation is continuous, corresponding to an idealized one-dimensional photonic crystal. The curve labeled "no hole" (black line) represents the case in which there is no perforation at all, and instead a large cavity is formed in the waveguide. This geometric configuration causes the localization of a low-frequency resonant mode due to the larger effective size of the void.

For this case, the maximum transmittance peak for the "no defect" waveguide is located at a relatively higher frequency compared to the circular shape defect. This clearly indicates that there is a geometry effect on the resonant frequency, although this effect is quite subtle. In particular, larger effective perforation size (in the case of a square shape) causes a pronounced effect on the electromagnetic field distribution

near this defect. This behavior is visible in the peak observed at $0.312[2\pi C/a]$, where the spacing between perforations in the waveguide becomes significant.

In the lower part of the frequency spectrum, the "no-hole" case produces a peak located at $0.251[2\pi C/a]$, indicating a resonance corresponding to the largest cavity size. This peak is characterized by a lower frequency compared to the circular perforation case due to its rectangular shape, which influences the overall cavity image and the resulting behavior of the resonant modes.

Configurations characterized by intermediate perforation sizes ranging from $r = 0.05$ to $r = 0.30$ reveal transmission peaks whose position and intensity gradually shift between these two extremes. As the square-shaped defect size increases, the peak frequency shifts toward higher frequencies, and the intensity exhibits a more complex and decidedly non-monotonic behavior. As can be seen, the intensity initially increases with defect size, having its peak at $r = 0.20$, and then gradually decreases, finally reaching a minimum for the "no defect" case.

These observations highlight the key role of defect geometry in shaping the photonic properties of the waveguide, with rectangular perforations showing a strong correlation between cavity size, resonant mode location, and the resonant frequency itself.

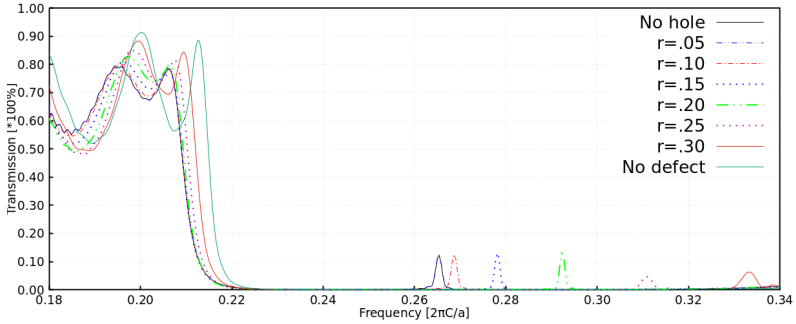

Fig. 3. Transmission for square-shape holes waveguide

In order to better understand how the shape and size of the central defect influence the spectral position of the transmission modes, Figure 4 presents the frequencies of the left and right transmission peaks as a function of defect size, for both circular and square hole geometries. The “left” and “right” peaks refer to the two distinct resonant modes that emerge within the normalized transmission spectra shown earlier, with the left peak generally appearing at lower frequencies and the right peak at higher frequencies.

Analysis of Figure 4 shows the same upward shift of both peaks with increasing defect size, regardless of the perforation shape. This behavior can be attributed to a decrease in the effective cavity volume with increasing defect size, which leads to an increase in the resonant frequency of the local mode. At the same time, as can be seen, both considered geometries, i.e., circular and square, exhibit similar behavior.

Therefore, it can be concluded that the key parameter controlling this shift is the defect size, while the defect shape is a parameter with a smaller, secondary influence.

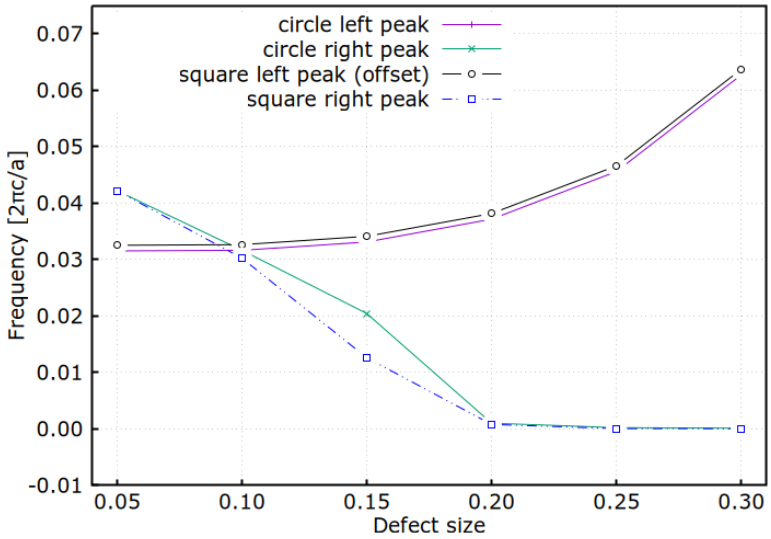

Fig. 4. Peak position shift of transmission modes as a function of defect size for circular and square perforation shapes

However, a subtle quantitative difference between the two geometries can be observed: for the same nominal defect size, square perforations tend to exhibit slightly higher frequency values than their circular counterparts. This is likely due to differences in the effective dielectric contrast and field distribution around the corners of the square holes, which may enhance field confinement and shift the mode slightly upward in frequency.

Because the data points corresponding to the left peaks for both shapes almost perfectly overlap, a small vertical offset was applied to the square left peak series in Figure 4 for visualization clarity. This ensures both trends remain distinguishable on the plot, while the physical meaning of the data remains unchanged.

Summarizing the above analysis, one can generally conclude that both defect location and symmetry play a significant role in shaping resonance properties of the waveguide. At the same time, defect size remains the dominant factor influencing the observed frequency shift.

4. Conclusions

In this paper, we investigated the influence of defect geometry and size on the transmission of an electromagnetic wave through a photonic waveguide. For this defect, we chose circular and rectangular shapes of perforation. Then, taking into

account different types of defects, normalized transmission spectra were determined and compared with the structure without perforations.

Detailed analysis showed that introducing a defect in the waveguide structure causes the appearance of localized transmission modes located in the frequency range between $0.24[2\pi C/a]$ and $0.32[2\pi C/a]$. At the same time, it was noticed that the position of these resonant modes depends mainly on the size of the considered defect, causing the resonance peaks to shift towards higher frequencies with increasing defect size. As shown, this is mainly caused by the reduction of the effective void volume which consequently leads to an increase in the resonance frequency. Since this frequency shift occurs for both square and circular perforations, it can be concluded that size is the dominant factor in electromagnetic wave transmission. At the same time, the contribution of perforation shape cannot be entirely ruled out, since the perforation geometry has been observed to influence the appearance of resonant modes at higher frequencies in the case of square perforations compared to circular perforations of equal size. Such differences can be induced by the sharp edges of perforations of square shape (which are naturally absent in circular perforations) and which represent significant modifications to the local distribution of the electromagnetic field near the perforations.

The analysis conducted during the study revealed that the normalized transmission intensity changes in a complex manner with increasing defect size. In the first phase, when the defect size is small, transmission increases with its size until reaching a maximum associated with the specific defect size. Then, as the defect size increases further, the trend reverses and transmission decreases (even when the defect is completely removed). This indicates that a balance exists in the waveguide between the presence of resonant modes and the inevitable leakage of electromagnetic wave energy. This highlights the crucial role of waveguide geometry in optimizing transmission for the studied range of electromagnetic radiation.

To conclude, the study demonstrates that both the size and shape of waveguide defects can be effectively used in the design and optimization for the required nature of the wave transmission. In the near future, this could be used to build precisely tuned filters or resonators that will be highly selective and allow for precise control of the system's transmission properties. At the same time, the method for achieving these desired properties is straightforward and easy to implement.

References

[1] Yu, W., Liu, S., Sun, H., Wang, J., Yang, Y., & Shen, X. (2025). Multiband adjustment engineering strategy for broadband range in photonic crystals. *Results in Physics*, *68*, 108104.

[2] Gao, Y.F., Sun, M.Y., Yao, T.H., Li, S.Y., Zhou, S.Y., Yang, M., & Hou, Q.C. (2025). Realization of multifunctional optical devices based on valley topological photonic crystals with triangular lattice. *Optics Communications*, *579*, 131549.

[3] Pardo, O.D., & Rey-González, R.R. (2025). Photonic band gap atlas, formula extension, and design applications in 1D photonic crystals. *Photonics and Nanostructures-Fundamentals and Applications*, *63*, 101355.

[4] Ragonese, A., & Nouh, M. (2021). Prediction of local resonance band gaps in 2D elastic metamaterials via Bloch mode identification. *Wave Motion*, *105*, 102734.

[5] Gruszka, K.M., & Dośpiał, M. (2022). Optical properties of two-dimensional dielectric perforated waveguide with variable hole-type defect. *Acta Physica Polonica: A*, *142*(1).

[6] Bingi, J., Nair, R.V., & Vijayan, C. (2017). Time dependent Bloch mode transmittance in self-assembled random photonic crystal for photonic time delay switching. *Optical Materials*, *64*, 95-99.

[7] Afkir, N.B., Er-rafyg, A., & Sekkat, Z. (2024). Broadband light absorption enhancement in a-Si: H ultrathin film solar cells with nanophotonic light trapping structures. *Materials Today Communications*, *40*(1), 109595.

[8] Qiu, M., & He, S. (2001). Surface modes in two-dimensional dielectric and metallic photonic band gap structures: a FDTD study. *Physics Letters A*, *282*(1-2), 85-91.

[9] Rafiee, E. (2024). A 2-D based photonic crystal biosensor for efficient diagnosis of anemia and kidney failure. *Optical Materials*, *149*, 115154.

[10] ur Rehman, A., Khan, Y., Ahmed, U., Irfan, M., Amirzada, M.R., & Butt, M.A. (2024). A comparative study of the photonic crystals-based cavities and usage in all-optical-amplification phenomenon. *Photonics and Nanostructures-Fundamentals and Applications*, *61*, 101298.

[11] Houle, J., & Sullivan, D. (2019). *Electromagnetic Simulation Using the FDTD Method with Python*. Wiley-IEEE Press.